Geophysical Journal International

Geophys. J. Int. (2016) **206,** 1634–1644
Advance Access publication 2016 June 24
GJI Seismology

doi: 10.1093/gji/ggw235

Higher-mode ambient-noise Rayleigh waves in sedimentary basins

Yiran Ma, Robert W. Clayton and Dunzhu Li

Seismological Laboratory, California Institute of Technology, Pasadena, CA 91125*, USA. E-mail: yrma@caltech.edu*

Accepted 2016 June 20. Received 2016 June 18; in original form 2016 January 21

SUMMARY

We show that higher modes are an important component of high-frequency Rayleigh waves in the cross-correlations over sedimentary basins. The particle motions provide a good test for distinguishing and separating the fundamental from the first higher mode, with the fundamental mode having retrograde and the first higher mode having prograde motion in the 1–10 s period of interest. The basement depth controls the cut-off period of the first higher mode, which coincides with a rapid increase (over period) in the particle-motion ellipticity or H/V ratio of the fundamental mode. The strong higher mode we observed is not only due to the low-velocity sedimentary layer but also due to the noise sources with significant radial component such as the basin edge scattering. It is important to correctly identify the mode order when inverting the dispersion curves because misidentifying the higher mode as fundamental will lead to an anomalous high V_{SV} velocity.

Key words: Interferometry; Surface waves and free oscillations; Wave propagation.

1 INTRODUCTION

Determining the basin structure is important for evaluating the potential seismic hazard because basins trap and amplify strong motion energy (Olsen 2000; Komatitsch *et al.* 2004). The Los Angeles Basin is a typical example of this, where there have been many studies of its structure (Hauksson & Haase 1997; Fuis *et al.* 2001; Süss & Shaw 2003; Tape *et al.* 2009; Lee *et al.* 2014; Shaw *et al.* 2015), using data from both passive and active seismic experiments, as well as well-logs and reflection data from the oil industry. The culmination of these efforts has been the creation of a series of steadily improving Community Velocity Models (Kohler *et al.* 2003; Plesch *et al.* 2011; Shaw *et al.* 2015), which are used among other things, in the simulation of ground motions from scenario earthquakes.

Methods based on ambient noise cross-correlation (Shapiro *et al.* 2005; Yao *et al.* 2006; Lin *et al.* 2008, 2014) have been an important development in building basin models. With a dense recording array, both high-frequency surface waves (Lin *et al.* 2013; Shirzad & Shomali 2014; Fang *et al.* 2015) and body wave signals (Nakata *et al.* 2015) can be extracted, and used to determine the structure. The ellipticity of the Rayleigh-wave particle motion is also being measured (Savage *et al.* 2013) which can be used to infer the depth of the basin. The generation of empirical Green's functions by correlation can be used to generate scenario earthquakes, which when compared to numerical simulations can be used to test the basin models (Denolle *et al.* 2013, 2014).

One problem that arises when using ambient-noise surface waves to determine structure of basins is the presence of higher modes. The standard analysis generally assumes that the fundamental mode is dominant in the vertical component cross-correlations. While this is generally true for regional scale surveys, there are cases where the higher-mode Rayleigh wave can also be strong (Savage *et al.* 2013; Rivet *et al.* 2015). A misidentification of the mode can lead to a higher V_{SV} and incorrect anisotropy estimates (V_{SV} versus V_{SH}), as well as incorrect amplitude information.

In this paper, we analyse surface waves generated by ambient-noise correlations using data from a dense broad-band array that was deployed across the Los Angeles Basin. The density of the array allows us to clearly see the modes and to measure their properties. The actual model of the basin that is determined will be the subject of another paper (Ma & Clayton 2016) where the surface wave dispersion curves are combined with receiver functions to measure the shape and velocity structure of the Los Angeles Basin.

Fig. 1 shows the location of the dense array comprised of 73 three-component broad-band seismometers, and the CVM-H model along the profile. Of particular interest in this paper are 44 (of 73) stations that are deployed in a linear array with ∼1 km interstation distance. They were operational from September to November 2014, with an average recording time of about 40 d. This 'high-density short-duration' experiment, named the 'Los Angeles Syncline Seismic Interferometry Experiment' (LASSIE), turns out to be effective for the ambient-noise studies and may serve as a prototype experiment that will allow basins to be covered by this type of low-cost short-duration survey.

2 MULTI-COMPONENT CROSS-CORRELATIONS

Following methods of Bensen *et al.* (2007) and Lin *et al.* (2014), we perform cross-correlations between all three components of each pair of stations. The Green's function can be approximated by the

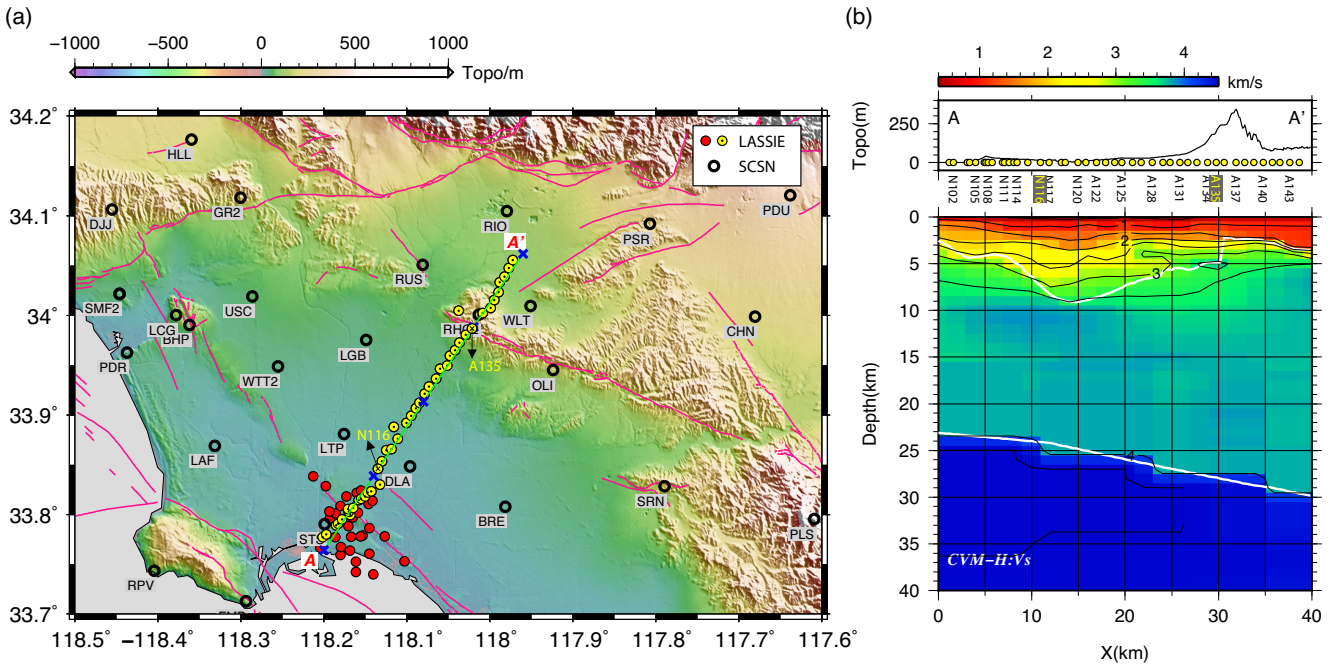

Figure 1. (a) The LASSIE array. The red and yellow dots are LASSIE stations, and the black circles are SCSN stations. The green line denotes the location of the 2-D profile (A–A′), and the distances from 'A' are marked with blue crosses in 10 km intervals. The faults are shown with pink lines (from Jennings & Bryant 2010). (b) CVM-H model along A–A′ profile. The white lines delineate the basement and the Moho depths. The Puente Hills is at ∼30 km distance, and separate the Los Angeles Basin to the south and the San Gabriel Valley to the north.

negative of the time derivative of the cross-correlation with the positive and negative time lags stacked. Either of the two stations can be the 'virtual source', and the other is the 'receiver', with the source or receiver component being the one used in the cross-correlation. In the following, we take the cross-correlations between N116 and all the linear-array stations (yellow dots in Fig. 1) as examples. *R*, *T* and *Z* refer to the radial, tangential and vertical component, respectively, and H/V is the ratio between the horizontal and vertical radius of the Rayleigh-wave particle-motion ellipse.

Before the cross-correlations, the data (cut to 1-d segments) for each station are pre-processed (Bensen *et al.* 2007) to enhance the surface wave signals. As in Lin *et al.* (2014), the same trace is used for all the three components in the time domain normalization or spectral whitening steps in the pre-processing, so that the H/V (R/Z) ratio is preserved for each Rayleigh-wave arrival. The Rayleigh-wave H/V ratio is a site property which is controlled solely by the local structure beneath the receiver (Tanimoto & Rivera 2008; Yano *et al.* 2009; Lin *et al.* 2014), and therefore is same for all the Rayleigh-wave arrivals over time regardless of their propagation paths. This guarantees that the Rayleigh wave in the cross-correlation (e.g. measured from *Z–R* and *Z–Z* cross-correlations) also has its H/V ratio preserved (see Appendix A).

The Love wave emerges from the tangential-component (*T–T*) cross-correlations. Clear Love wave signals are observed along the 1-s period profile in Fig. 2(a) and 5-s period profile in Supporting Information Fig. S1, except in the 1-s period for those stations located at a distance beyond 30 km. In Fig. 2(b), we take the cross-correlation between N116 and A138 as an example. It shows that the noise in the 1-s period cross-correlation is persistent regardless of the number of days used in the cross-correlation. Note that the Puente Hills is located at the 30 km point in the A–A′ profile (Fig. 1), and the noisy signals are likely due to the scattering effect of the topography, which can produce strong precursor and coda waves (Ma *et al.* 2013).

The Rayleigh wave emerges from the vertical (*Z*) and radial (*R*) component cross-correlations. Fig. 3 shows the *Z–Z* and *R–Z* cross-correlations filtered to 1-s period with a Gaussian filter. The *Z–Z*, *Z–R*, *R–Z* and *R–R* cross-correlations filtered to 1-, 3- and 5-s periods are shown in Supporting Information Fig. S2. Using station N116 as the virtual source, we see in the 1-s period profiles (Fig. 3 and Supporting Information Fig. S2a) that the fundamental and higher-mode Rayleigh waves are equally strong with a *Z*-directed force at N116 (i.e. *Z–Z* and *Z–R* cross-correlations). The higher mode is even stronger than the fundamental mode with an R-directed force (i.e. *R–Z* and *R–R* cross-correlations) as is also observed in Savage *et al.* (2013). The higher mode dominates at 3-s period (Supporting Information Fig. S2b), but it is evanescent in the 5-s period profiles (Supporting Information Fig. S2c), where only the fundamental mode is observed.

Using the multi-component cross-correlations between two stations, we can show the particle motion of the two modes at the two station sites. The positive and negative lags of the cross-correlations are stacked to approximate the Green's function. We take the cross-correlations between N116 and A135 as an example, and the results are shown in Figs 4(a) and (b). N116 is located in the basin while A135 in the Puente Hills (Fig. 1). In Figs 4(a) and (b), we also annotate the pair of cross-correlations used for each particle motion measurement, and the corresponding force direction at the virtual source. For example, using *Z–Z* and *Z–R* cross-correlations, which correspond to a *Z*-directed force at N116, we can measure the particle motion at A135. Using the *Z–Z* and *R–Z* cross-correlations, which correspond to a *Z*-directed force at A135, we can measure the particle motion at N116. Note that the sign of the *R–Z* cross-correlation needs to be inverted since the *R* direction (from A135 to N116) is opposite to that in the cross-correlation (from N116 to A135). We use a time window of one wavelength centred at the peak of the envelope to measure the particle motion. The particle motion

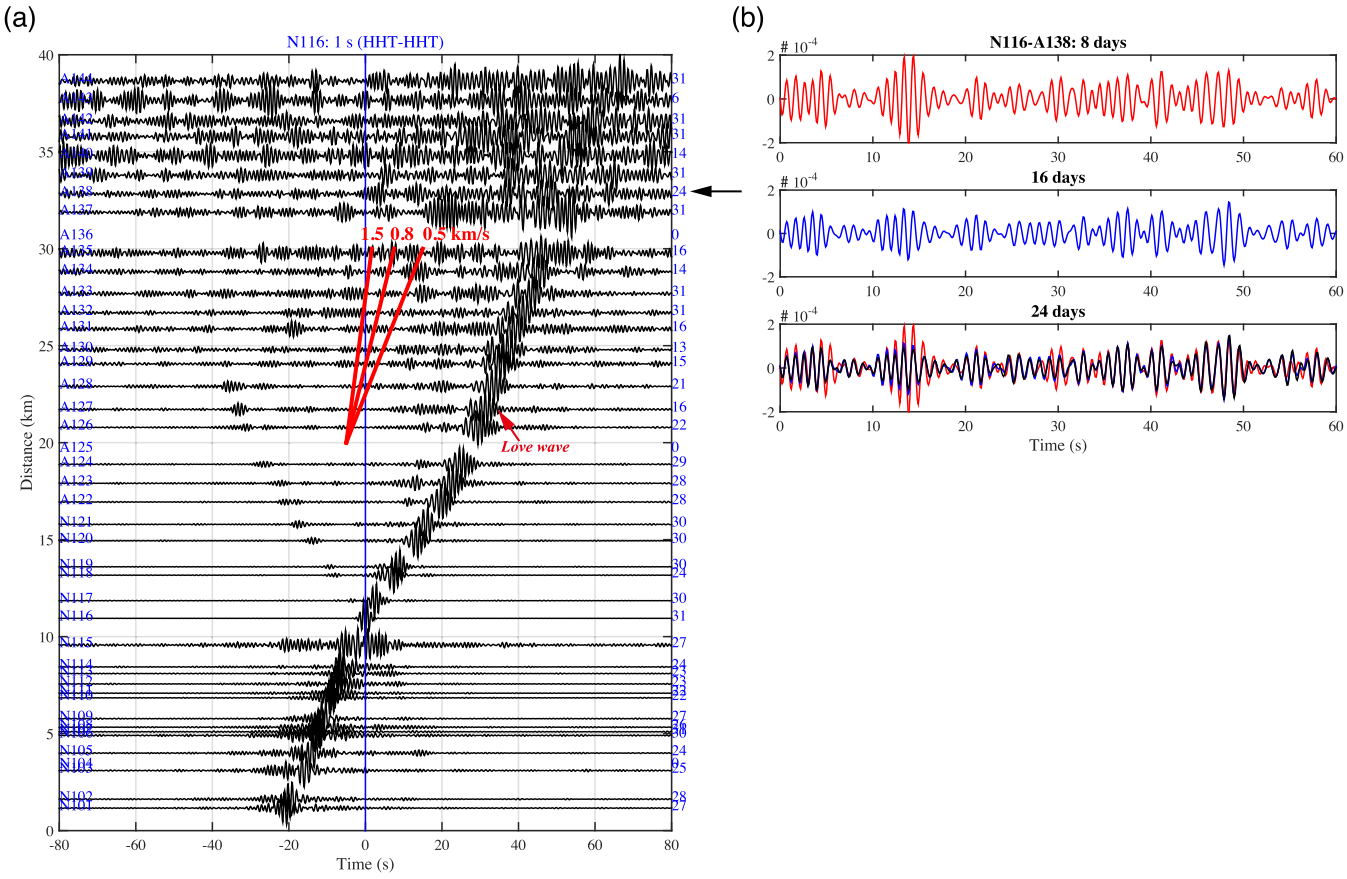

Figure 2. (a) Love wave shown in the tangential-component cross-correlations between N116 and all the yellow stations in Fig. 1. The *y*-axis shows the distances of the stations from A along A–A′ profile (Fig. 1). The number of days used in each cross-correlation is annotated in blue. The cross-correlations filtered to 1-s period are shown here as examples. 5-s period examples are shown in Supporting Information Fig. S1. The Love wave signals are clear except for stations located at distances beyond 30 km. (b) The cross-correlation (also filtered to 1-s period) between N116 and A138 with 8 (in red), 16 (in blue) and 24 (in black) d of data. The third panel shows that the cross-correlations with 16 and 24 d of data are identical. The noise that is persistent in the cross-correlation can be related to the scattering effect of the Puente Hills located at the 30 km point in the A–A′ profile (Fig. 1).

ellipse is colour shaded with the time to show the direction of motion.

Figs 4(a) and (b) show the particle motions measured for different modes at different periods. The measurements with different source directions (Z or R) generally give similar results. There are gaps in our measurements, because we only measure when observe clear signals arriving at same time (same mode) in the cross-correlation pair. We observe that: (1) higher mode shows prograde particle motion, while the fundamental mode is retrograde, and (2) the higher mode disappears around 4 s, and above this 'cut-off period' the fundamental mode in the basin (N116) shows high ellipticity or H/V ratio.

We also note that the particle motion ellipse is not strictly upright as expected for a Rayleigh wave. This phenomenon is not specific to this study and is also shown in Lin *et al.* (2014, fig. 2 therein). In Section 4, we will show that the tilted ellipse is readily explained by body wave interference.

3 RAYLEIGH WAVES IN A BASIN MODEL

Some of the Rayleigh-wave observations can be explained with a 1-D basin model. The Rayleigh-wave Green's function in a 1-D layered structure is (Aki & Richards 2002):

$$G = \begin{bmatrix} G_{RR} & G_{RZ} \\ G_{ZR} & G_{ZZ} \end{bmatrix}$$
$$= \sum_n \frac{1}{8cUI_1} \begin{bmatrix} r_1(z)r_1(h) & -ir_1(z)r_2(h) \\ ir_2(z)r_1(h) & r_2(z)r_2(h) \end{bmatrix}$$
$$\times \left(\frac{2}{\pi k_n \Delta}\right)^{1/2} \exp\left[i\left(k_n\Delta + \frac{\pi}{4}\right)\right], \quad (1)$$

where n denotes the nth mode, h is the depth of the point source, z is the depth of the receiver, Δ is the distance between source and receiver; r_1 and r_2 are the horizontal and vertical displacement eigenfunctions (of the nth mode), k_n is the wavenumber of the nth mode, c and U are the phase and group velocity (of the nth mode) respectively, and $I_1 = \frac{1}{2}\int_0^\infty \rho(r_1^2 + r_2^2)\mathrm{d}z$ is the energy integral. What we observed are the fundamental ($n = 0$) and the first higher mode ($n = 1$). Note that the higher mode discussed in this paper refers to the first higher mode.

We see that for each mode, the particle motion ellipse is determined by $r_1(z = 0)$ and $r_2(z = 0)$ at the receiver, and the dependence of the wave amplitude on the source depth or direction (R or Z) is also controlled by the eigenfunctions $r_1(h)$ or $r_2(h)$. In Aki & Richards (2002), the positive Z-direction is downward, and as a result,

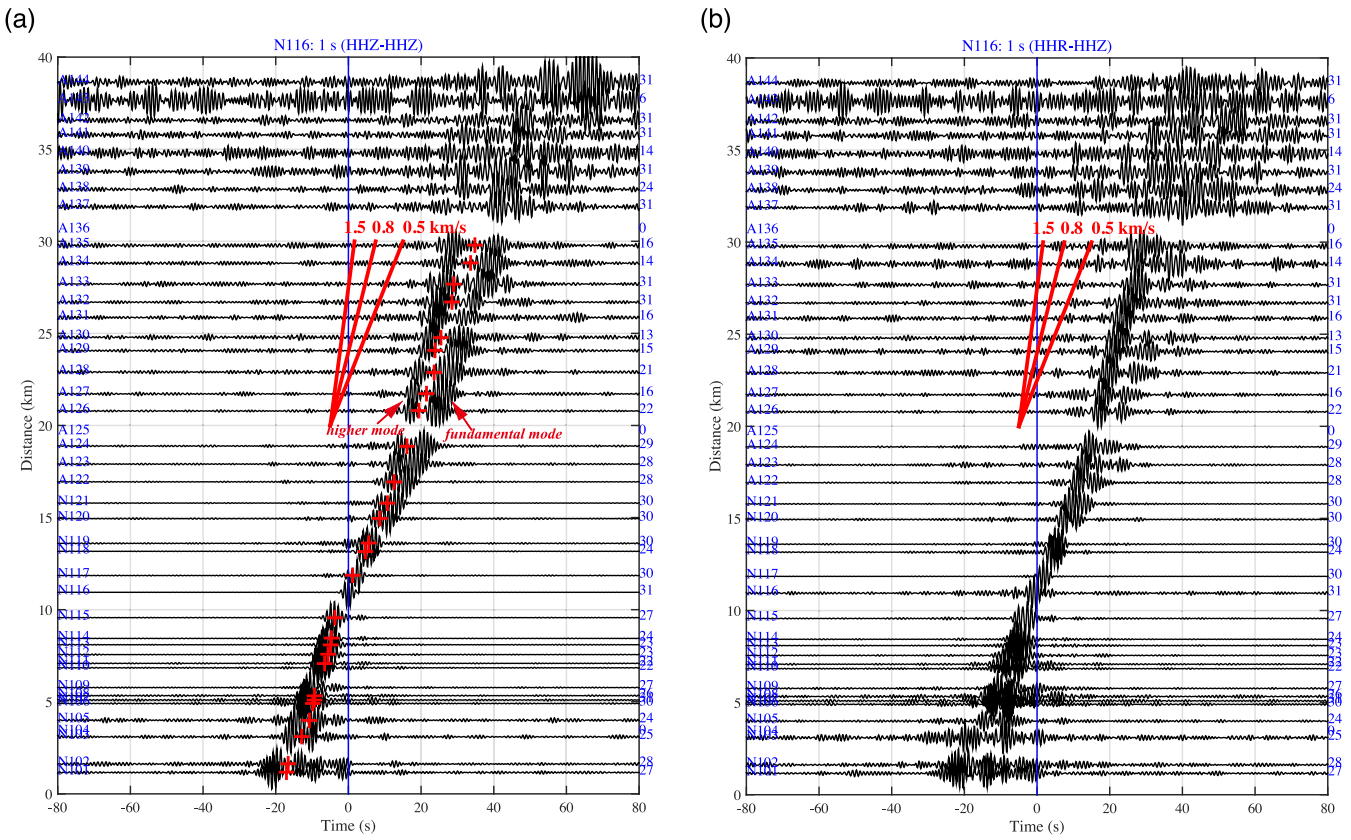

Figure 3. Fundamental and higher-mode Rayleigh waves shown in the vertical and radial component cross-correlations between N116 and all the yellow stations in Fig. 1. *Z*–*Z* and *R*–*Z* cross-correlations filtered to 1-s period are shown here as examples. More examples are shown in Supporting Information Fig. S2. The *y*-axis shows the distances of the stations from A along A–A′ profile (Fig. 1). The number of days used in each cross-correlation is annotated in blue. The red marker in (a) denotes the separation point between the fundamental and higher modes, using method described in Section 4.

opposite sign of r_1 and r_2 represents retrograde particle motion. However, we note that in our analysis, the positive *Z*-direction is upward, and therefore, the same sign represents retrograde particle motion. It is also the convention for the synthetics in this paper. The different sign convention is also discussed in Aki & Richards (2002, Box 7.10 therein).

Using the program from Herrmann & Ammon (2002), we can calculate the eigenfunctions and ellipticity for different 1-D basin models. An example for a simple basin model with parameters described in Table 1 is shown in Figs 4(c) and (d). The basement depth of 4 km is comparable to the average depth in the study region. It is shallower than that beneath N116 in CVM-H model (∼7 km in Fig. 1), but better fits the 4-s cut-off period of the higher mode.

From the eigenfunctions at 3-s period (Fig. 4c), we see that the particle motion at the surface differs in sign for the two modes. In addition, we see that the *R*-directed force can generate a stronger higher mode than *Z*-directed force, especially at greater depths, since r_1 decreases more slowly with depth than r_2 in 0–3 km depth range. The ellipticity over 1-10 s periods is shown in Fig. 4(d). In Supporting Information Fig. S3, we show similar plots for models with 6 and 8-km basement depths, and we see that distinct from the retrograde particle motion of the fundamental mode, the higher mode shows a prograde particle motion. The retrograde particle motion of higher mode only appears in the short period end (around 1-s period) in the 6 and 8-km depth basement models (Supporting Information Fig. S3). Therefore, the difference in the direction of particle motion, as is also evident in the data, can be useful to distinguish between the two modes in the 1–10 s period of interest.

In Fig. 4(d), we also note that at ∼4-s period (T_0), the higher mode disappears as shown by the truncation of the dispersion curve, which means no k_1 is found for the eigenproblem. It coincides with a rapid increase in the ellipticity of the fundamental mode (Fig. 4d), which is also shown in the observation (Fig. 4b). The cut-off period of the higher mode (T_0) can be estimated from the peak of the ellipticity of the fundamental mode (T_1), and both of them are controlled by the basement depth. This relationship is also shown in Supporting Information Fig. S3. However, in reality the structure is not 1-D, the cut-off period of the higher mode is more likely to be related to some average of the basement depth of the basin, while the fundamental-mode particle-motion ellipticity is related to the basement depth in the local site. For example, there is no such relationship between the fundamental and higher mode in Fig. 4(a), in which the receiver is at the Puente Hills. Nevertheless, using the receiver at the basin as in Fig. 4(b) gives a good estimate of T_0 from the fundamental mode.

The relative amplitude of the two modes is not only controlled by the structure between the two stations or the channels used in the cross-correlations (i.e. the Green's function), but also the relative amplitude of the two modes generated by the noise sources (Snieder 2004). It is similar to the effect that an anisotropic distribution of noise sources causes asymmetry in the cross-correlation (e.g. Fig. 2a due to strong noise sources at the ocean side). We use the FK method (Zhu & Rivera 2002) to compute synthetics for the model in Table 1, with a point source (*R*- or *Z*-directed force) with central period of 3 s at 0.5 km depth. For a *Z*-directed source, the fundamental mode is dominant, even with a basin model.

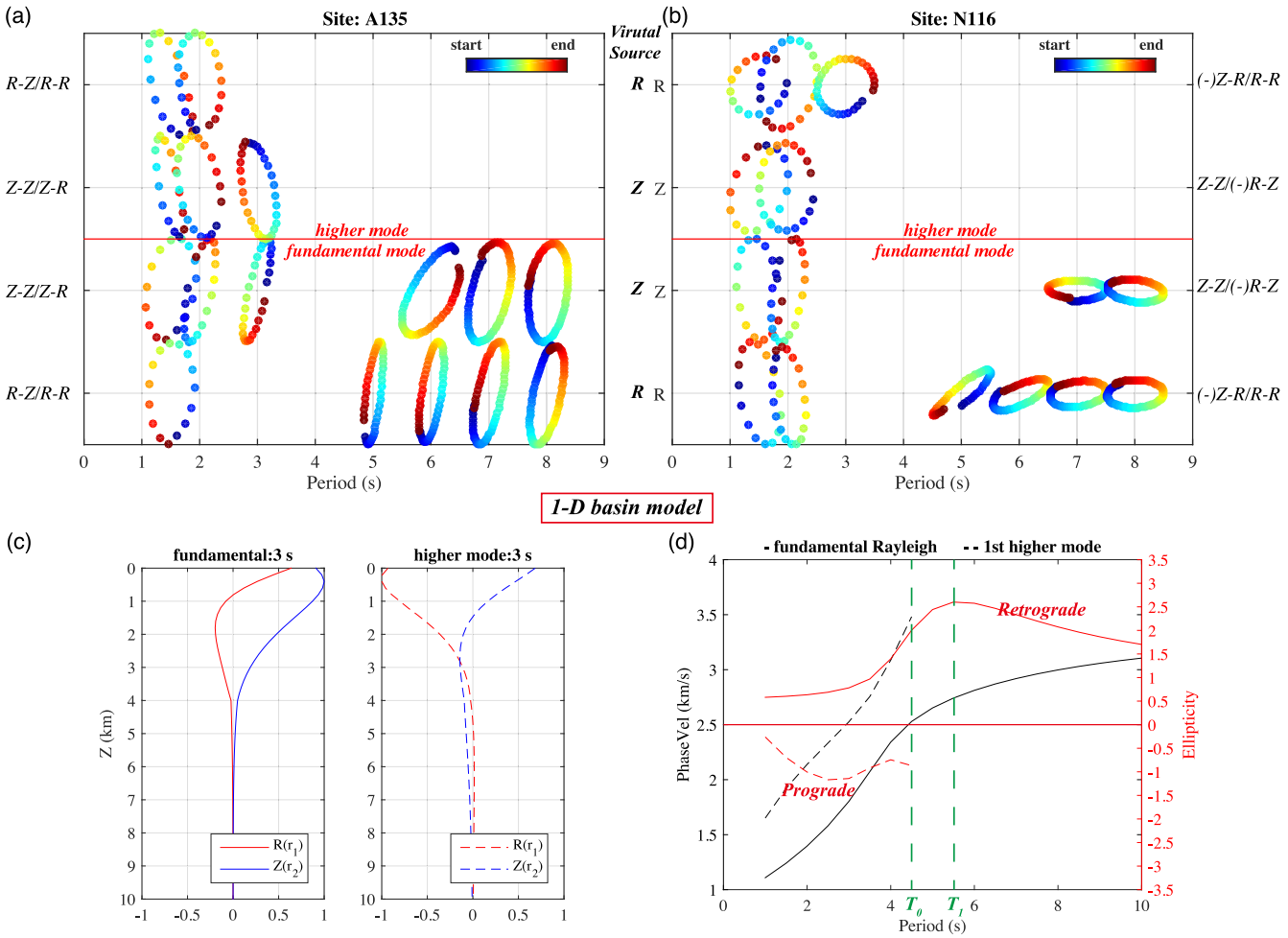

Figure 4. Panels (a) and (b) show the particle motion measurements using the cross-correlations (*Z–Z*, *Z–R*, *R–R*, *R–Z*) between N116 and A135. N116 is located in the basin while A135 in the Puente Hills (Fig. 1). For each period, we have a maximum of four measurements corresponding to the two force directions at the virtual source and two modes. We only measure the particle motion when the phase is clear. The higher mode disappears above ∼4-s period. The higher mode has a prograde particle motion, while the fundamental mode has a retrograde particle motion. A rapid increase in the ellipticity of the fundamental mode around 4-s period is observed at N116. The observations can be explained with a 1-D basin model in Table 1. Panel (c) shows the eigenfunctions of this model, and panel (d) shows the phase velocity and particle-motion ellipticity (H/V) versus period. T_0: cut-off period of the higher mode; T_1: period having maximum fundamental-mode ellipticity.

Table 1. 1-D basin model.

	H (km)	V_S (km s^{-1})	V_P (km s^{-1})	Rho (g cm^{-3})
Sediments	4	1.0–3.0 (gradient)	2.5–5.0	2.0–2.5
Half space		3.8	6.5	2.8

Therefore, the Green's function of a 1-D basin model cannot explain the strong higher mode we observe in the *Z–Z* cross-correlations. Strong higher mode is generated by an *R*-directed source in a basin model (Supporting Information Fig. S4). Thus, we deduce that those noise sources that are effectively *R*-directed contribute to the strong higher mode in the cross-correlation. Considering the asymmetry of the cross-correlation and the 1–5 s period band discussed here, the primary noise sources are the secondary microseism (Longuet-Higgins 1950) that is equivalent to a vertical force (Gualtieri *et al.* 2013; Tanimoto *et al.* 2015). In contrast, the basin edge scattering has a significant horizontal component and can be important in generating the higher mode. The location of the edge of the LA Basin is evident from the basement depth map shown in Süss & Shaw (2003).

4 DISCUSSION

We see that with about 1-km interstation distance, we can extract strong surface wave signals as high as 1-Hz in frequency. The shorter period surface waves are sensitive to shallower depths, and therefore they are very useful to image the basin structure. Love wave signals are comparatively simple for dispersion analysis, but strong first higher-mode Rayleigh waves in the basin (e.g. Fig. 3) complicate the use of Rayleigh waves. The strong higher mode in the cross-correlation is not only due to the low-velocity sedimentary layer, but also the contribution from the R-directed noise sources, such as the basin edge scattering.

Rivet *et al.* (2015) recently proposed to use the H/V ratio to distinguish between the modes. Their work involves inverting the dispersion curve for the V_S model assuming separate cases as to whether the Rayleigh wave is a fundamental or higher mode. The H/V ratios (over a range of periods) are then calculated for the two cases, and the one that best matches the data is chosen. In contrast, our proposed method distinguishes the two modes directly by measuring particle motion from the data.

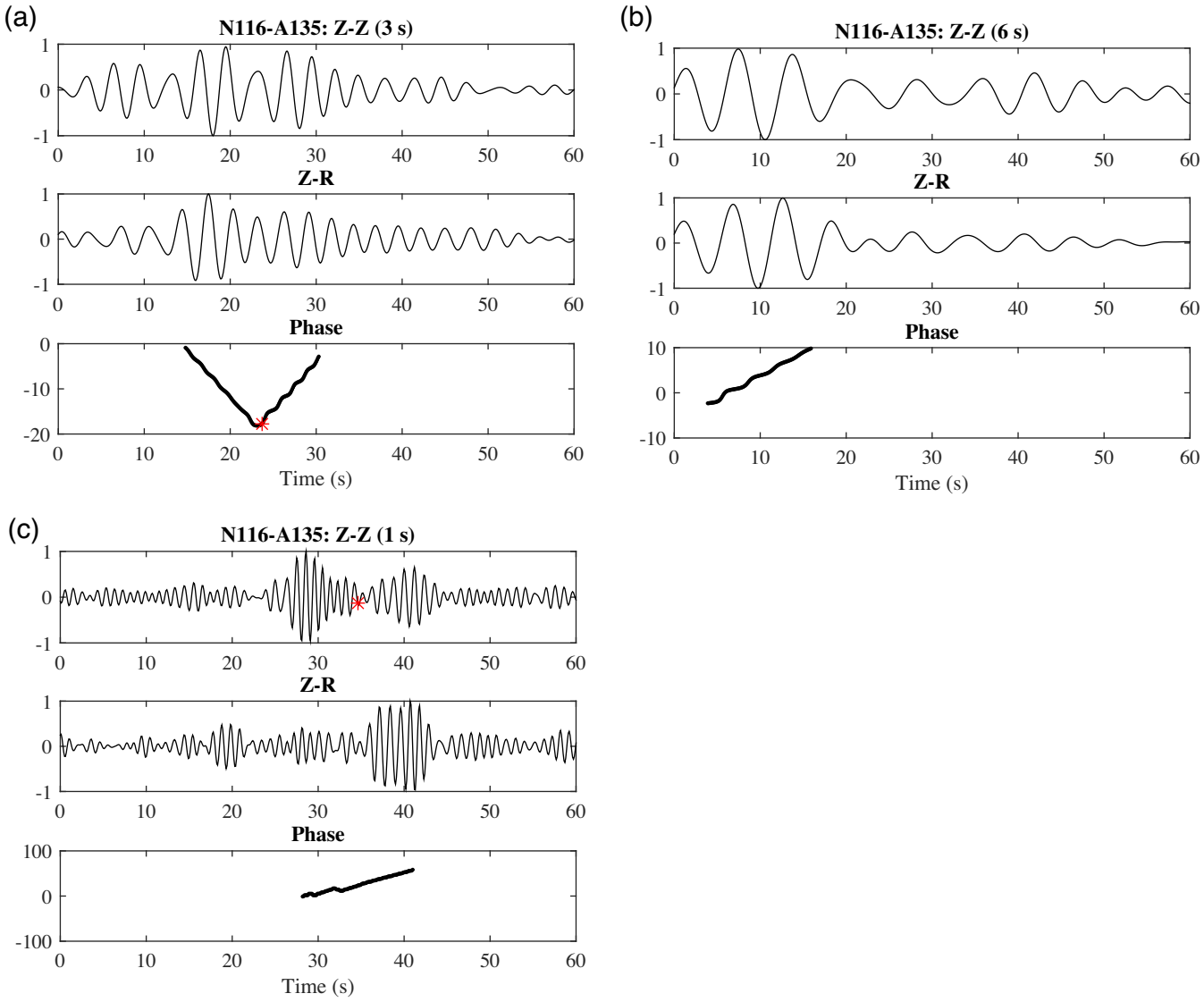

Figure 5. An example to distinguish the two modes using *Z–Z* and *Z–R* cross-correlations between N116 and A135. (a) At 3-s period. Both higher and fundamental modes are observed. The separation time corresponds to the maximum curvature point in the phase plot. (b) At 6-s period, only one mode is observed. The type as fundamental mode can be deduced from the slope of the phase plot. (c) At 1-s period, higher mode is only observed in *Z–Z* cross-correlation, indicating a near-zero ellipticity with possible change in sign. In this case, we can instead separate the modes at the middle of the two peaks in the envelope.

In Fig. 5, we show the examples using the *Z–Z* and *Z–R* cross-correlations between N116 and A135. We plot the (unwrapped) instantaneous phase $\phi(t) = \arg(r(t) + iz(t))$, with a 5-point (0.5 s) moving-window smoothing. We then calculate the instantaneous curvature $\phi''(t)$. The time t^*, which corresponds to the maximum of $\phi''(t)$, is where the two modes separate. The slope of $\phi(t)$ should be negative for $t < t^*$ (higher mode) and positive for $t > t^*$ (fundamental mode) (Fig. 5a). If we only observe one mode, then we can deduce its type by the slope (Fig. 5b). This method can fail at high frequency when the two modes have the same sign. In Fig. 5(c), at 1-s period, the higher mode is only clear in the *Z* component, indicating a near-zero ellipticity, which is at the point where it is changing sign to retrograde (e.g. Supporting Information Fig. S3). In this case we can alternatively separate the modes based on the envelopes. In Fig. 6, we show the separations of the modes based on the method described here. Note that among all the cross-correlations in the profile, N116-A135 is the only one that belongs to the third case (Fig. 5c). The fundamental mode can also have a prograde particle motion at high frequency (Denolle *et al.* 2012).

Denolle *et al.* (2012) examined the particle motion direction of the fundamental mode at six stations in the LA basin surroundings, and found prograde direction in periods less than 2 s for the CHN station (see Fig. 1 for the location), where the sediment thickness is less than 1 km. The fundamental mode particle motion can be prograde if the velocity gradient in the sedimentary layer is very large (Tanimoto & Rivera 2005; Denolle *et al.* 2012). Nevertheless, a retrograde particle motion of the fundamental mode is a more general phenomena, as shown in the other 5 stations located in the deeper part of the LA Basin in Denolle *et al.* (2012) as well as our results above.

The Rayleigh-wave particle-motion ellipse has an observable inclination, which can be explained by body wave interference. As shown in Appendix B, the summation of one surface wave and one

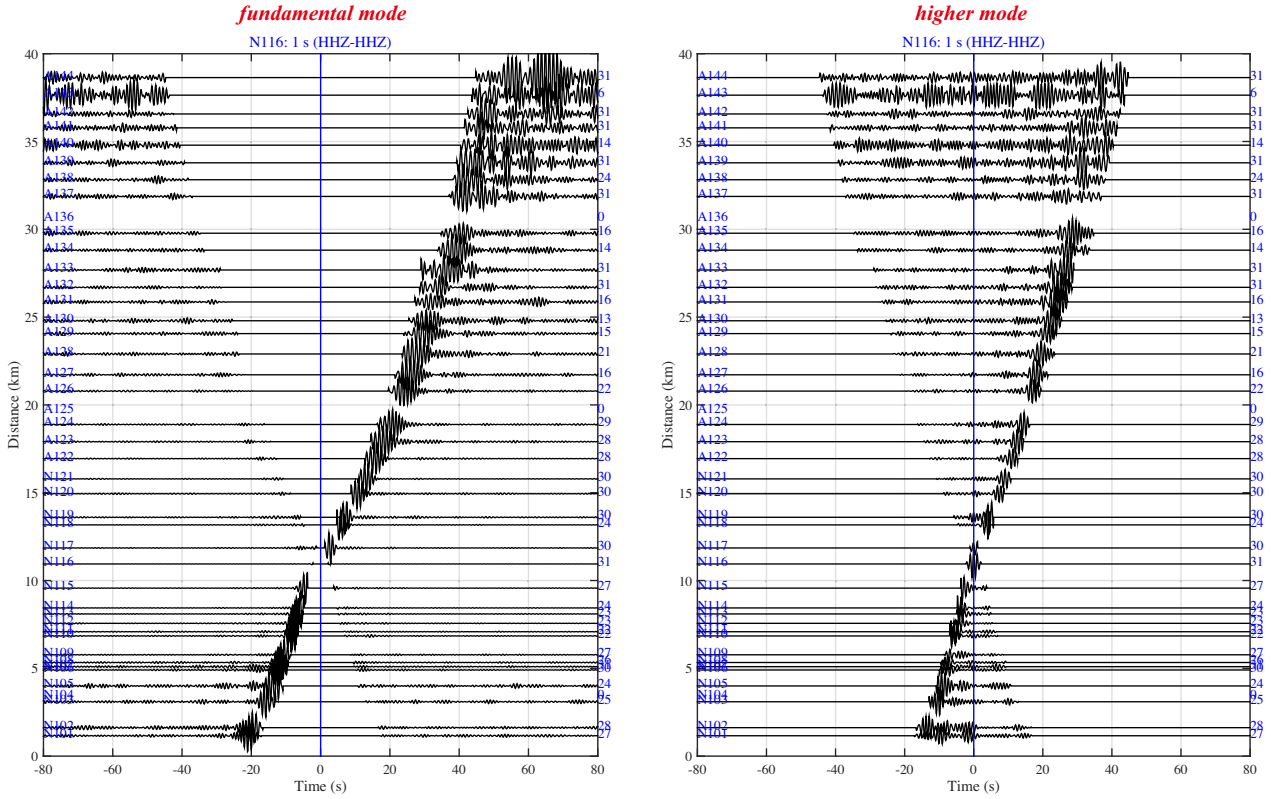

Figure 6. The separation of the fundamental and higher mode at 1-s period. The original figure is in Fig. 3(a). The separation points based on the method described in Section 4 are shown in red markers in Fig. 3(a). No separation points are found for stations beyond 30 km because of the noisy signals at 1-s period, and the separation is based on the extrapolation from the rest.

body wave with arbitrary phase can be written as

$$\begin{bmatrix} x(t) \\ y(t) \end{bmatrix} = M_{2\times2} \begin{bmatrix} \cos(wt+\phi) \\ \sin(wt+\phi) \end{bmatrix} = U_{2\times2}\Sigma_{2\times2}V^T_{2\times2} \begin{bmatrix} \cos(wt+\phi) \\ \sin(wt+\phi) \end{bmatrix}, \quad (2)$$

where M is related to the amplitudes and relative phase of the two waves; w is the angular frequency and $wt+\phi$ is the phase of the surface wave (without interference); U, V and Σ are the matrices of singular value decomposition of the M matrix, where U and V are orthonormal matrices, and Σ is a diagonal matrix.

We recognize that the particle motion described by $[\cos(wt+\phi); \sin(wt+\phi)]$ is a circle, V^T performs a rotation on the circle and the result remains a circle. The circle is then stretched to an ellipse with the operation of Σ, and finally, the ellipse is rotated by the operator U, which results in the tilted ellipse we observed. The surface and body waves, however, cannot be uniquely determined from the observed ellipse as we also show in Appendix B.

The cut-off period (T_0), above which the first higher mode disappears, is controlled by the basement depth. In a 1-D model, this period coincides with the rapid increase in the fundamental mode ellipticity (H/V ratio) and is close to the period ($T_1 = 1/f_1$) with the peak H/V ratio (Fig. 4d). The frequency f_1 approximates the resonance frequency of the basin (Nakamura 1989; Field & Jacob 1993; Fäh *et al.* 2001; Boaga *et al.* 2013) and is related to the basement depth (h) by $f_1 \approx V_S/2h$ from the constructive interference of shear waves. In reality the structure is not 1-D, but we can still use the fundamental mode ellipticity at the basin station to estimate T_0, with the assumption that the local basement depth is close to the average of the basin. For example, the data in Fig. 4(b) show the rapid change in the fundamental-mode ellipticity around 4-s period, which is about the T_0 shown there. It is also close to the T_1 estimated from a basement depth of 5 km (with $V_S = 2$ km s^{-1}), which is the average basement depth in CVM-H model (Fig. 1). Alternatively, we can estimate the period in which the higher mode exists from the known basement depth measured from other methods, such as receiver functions.

5 CONCLUSIONS

We show some characteristics of the Love and Rayleigh waves in the Los Angeles Basin, which emerge in the multi-component cross-correlations using data from the LASSIE experiment. While the Love wave is simple, the Rayleigh wave is complicated due to the strong first higher mode. The low-velocity sedimentary layer and the radial-component noise sources together explain the strong first higher mode in the observations. We show that the particle motion direction can be used to distinguish between the two modes in the 1–10-s period of interest. The cut-off period of the first higher mode is controlled by the basement depth, which coincides with the rapid increase in the H/V ratio of the fundamental mode.

ACKNOWLEDGEMENTS

We thank Mich Barklage and Dan Hollis from NodalSeismic, Paul Davis and Igor Stubailo from UCLA, Elizabeth Cochran from USGS, Jacha Polet from Cal Poly Pomona, and several grad students for their participation in the LASSIE experiment. We thank Victor Tsai at Caltech for useful discussions. We also thank two anonymous reviewers for their helpful comments. This work was partially

supported by the USGS Earthquake Science Center/Caltech Cooperative Agreement G14AC00109 and by SCEC award #15018.

REFERENCES

Aki, K. & Richards, P.G., 2002. *Quantitative Seismology,* University Science Books.

Bensen, G., Ritzwoller, M., Barmin, M., Levshin, A., Lin, F., Moschetti, M., Shapiro, N. & Yang, Y., 2007. Processing seismic ambient noise data to obtain reliable broad-band surface wave dispersion measurements, *Geophys. J. Int.,* **169**(3), 1239–1260.

Boaga, J., Cassiani, G., Strobbia, C.L. & Vignoli, G., 2013. Mode misidentification in Rayleigh waves: ellipticity as a cause and a cure, *Geophysics,* **78**(4), EN17–EN28.

Denolle, M., Dunham, E., Prieto, G. & Beroza, G., 2013. Ground motion prediction of realistic earthquake sources using the ambient seismic field, *J. geophys. Res.,* **118**(5), 2102–2118.

Denolle, M., Dunham, E., Prieto, G. & Beroza, G., 2014. Strong ground motion prediction using virtual earthquakes, *Science,* **343**(6169), 399–403.

Denolle, M.A., Dunham, E.M. & Beroza, G.C., 2012. Solving the surface-wave eigenproblem with Chebyshev spectral collocation, *Bull. seism. Soc. Am.,* **102**(3), 1214–1223.

Fäh, D., Kind, F. & Giardini, D., 2001. A theoretical investigation of average *H*/*V* ratios, *Geophys. J. Int.,* **145**(2), 535–549.

Fang, H., Yao, H., Zhang, H., Huang, Y.-C. & van der Hilst, R.D., 2015. Direct inversion of surface wave dispersion for three-dimensional shallow crustal structure based on ray tracing: methodology and application, *Geophys. J. Int.,* **201**(3), 1251–1263.

Field, E. & Jacob, K., 1993. The theoretical response of sedimentary layers to ambient seismic noise, *Geophys. Res. Lett.,* **20**(24), 2925–2928.

Fuis, G., Ryberg, T., Godfrey, N., Okaya, D. & Murphy, J., 2001. Crustal structure and tectonics from the Los Angeles basin to the Mojave Desert, southern California, *Geology,* **29**(1), 15–18.

Gualtieri, L., Stutzmann, E., Capdeville, Y., Ardhuin, F., Schimmel, M., Mangeney, A. & Morelli, A., 2013. Modelling secondary microseismic noise by normal mode summation, *Geophys. J. Int.,* **193**(3), 1732–1745.

Hauksson, E. & Haase, J.S., 1997. Three-dimensional VP and VP/VS velocity models of the Los Angeles basin and central Transverse Ranges, California, *J. geophys. Res.,* **102**(B3), 5423–5453.

Herrmann, R. & Ammon, C., 2002. *Computer Programs in Seismology: Surface Waves, Receiver Functions and Crustal Structure,* St. Louis University.

Jennings, C.W. & Bryant, W.A., 2010. Fault activity map of California: California Geological Survey, Geologic Data Map Series No. 6, map scale 1:750 000.

Kohler, M., Magistrale, H. & Clayton, R., 2003. Mantle heterogeneities and the SCEC reference three-dimensional seismic velocity model version 3, *Bull. seism. Soc. Am.,* **93**(2), 757–774.

Komatitsch, D., Liu, Q., Tromp, J., Süss, P., Stidham, C. & Shaw, J.H., 2004. Simulations of ground motion in the Los Angeles basin based upon the spectral-element method, *Bull. seism. Soc. Am.,* **94**(1), 187–206.

Lee, E.-J., Chen, P., Jordan, T.H., Maechling, P.B., Denolle, M.A. & Beroza, G.C., 2014. Full-3-D tomography for crustal structure in Southern California based on the scattering-integral and the adjoint-wavefield methods, *J. geophys. Res.,* **119**(8), 6421–6451.

Lin, F.-C., Moschetti, M.P. & Ritzwoller, M.H., 2008. Surface wave tomography of the western United States from ambient seismic noise: Rayleigh and Love wave phase velocity maps, *Geophys. J. Int.,* **173**(1), 281–298.

Lin, F.-C., Li, D., Clayton, R.W. & Hollis, D., 2013. High-resolution 3D shallow crustal structure in Long Beach, California: application of ambient noise tomography on a dense seismic array, *Geophysics,* **78**(4), Q45–Q56.

Lin, F.-C., Tsai, V.C. & Schmandt, B., 2014. 3-D crustal structure of the western United States: application of Rayleigh-wave ellipticity extracted from noise cross-correlations, *Geophys. J. Int.,* **198**(2), 656–670.

Longuet-Higgins, M.S., 1950. A theory of the origin of microseisms, *Phil. Trans. R. Soc. A,* **243**(857), 1–35.

Ma, Y. & Clayton, R.W., 2016. Structure of the Los Angeles Basin from ambient noise and receiver functions, *Geophys. J. Int.,* doi:10.1093/gji/ggw236.

Ma, Y., Clayton, R.W., Tsai, V.C. & Zhan, Z., 2013. Locating a scatterer in the active volcanic area of Southern Peru from ambient noise cross-correlation, *Geophys. J. Int.,* **192**(3), 1332–1341.

Nakamura, Y., 1989. A method for dynamic characteristics estimation of subsurface using microtremor on the ground surface, *Q. Rep. Railw. Tech. Res. Inst.,* **30**(1), 25–33.

Nakata, N., Chang, J.P., Lawrence, J.F. & Boué, P., 2015. Body wave extraction and tomography at Long Beach, California, with ambient-noise interferometry, *J. geophys. Res.,* **120**(2), 1159–1173.

Olsen, K., 2000. Site amplification in the Los Angeles basin from three-dimensional modeling of ground motion, *Bull. seism. Soc. Am.,* **90**(6B), S77–S94.

Plesch, A., Tape, C., Graves, R., Small, P., Ely, G. & Shaw, J., 2011. Updates for the CVM-H including new representations of the offshore Santa Maria and San Bernardino basin and a new Moho surface, in *2011 Southern California Earthquake Center Annual Meeting, Proceedings and Abstracts,* vol. 21, p. 214.

Rivet, D., Campillo, M., Sanchez-Sesma, F., Shapiro, N.M. & Singh, S.K., 2015. Identification of surface wave higher modes using a methodology based on seismic noise and coda waves, *Geophys. J. Int.,* **203**(2), 856–868.

Savage, M.K., Lin, F.-C. & Townend, J., 2013. Ambient noise cross-correlation observations of fundamental and higher-mode Rayleigh wave propagation governed by basement resonance, *Geophys. Res. Lett.,* **40**(14), 3556–3561.

Shapiro, N.M., Campillo, M., Stehly, L. & Ritzwoller, M.H., 2005. High-resolution surface-wave tomography from ambient seismic noise, *Science,* **307**(5715), 1615–1618.

Shaw, J.H. *et al.*, 2015. Unified Structural Representation of the southern California crust and upper mantle, *Earth planet. Sci. Lett.,* **415,** 1–15.

Shirzad, T. & Shomali, Z.H., 2014. Shallow crustal radial anisotropy beneath the Tehran basin of Iran from seismic ambient noise tomography, *Phys. Earth planet. Inter.,* **231,** 16–29.

Snieder, R., 2004. Extracting the Green's function from the correlation of coda waves: a derivation based on stationary phase, *Phys. Rev. E,* **69**(4), 046610, doi:10.1103/PhysRevE.69.046610.

Süss, M.P. & Shaw, J.H., 2003. P wave seismic velocity structure derived from sonic logs and industry reflection data in the Los Angeles basin, California, *J. geophys. Res.,* **108**(B3), doi:10.1029/2001JB001628.

Tanimoto, T. & Rivera, L., 2005. Prograde Rayleigh wave particle motion, *Geophys. J. Int.,* **162**(2), 399–405.

Tanimoto, T. & Rivera, L., 2008. The ZH ratio method for long-period seismic data: sensitivity kernels and observational techniques, *Geophys. J. Int.,* **172**(1), 187–198.

Tanimoto, T., Hadziioannou, C., Igel, H., Wasserman, J., Schreiber, U. & Gebauer, A., 2015. Estimate of Rayleigh-to-Love wave ratio in the secondary microseism by colocated ring laser and seismograph, *Geophys. Res. Lett.,* **42**(8), 2650–2655.

Tape, C., Liu, Q., Maggi, A. & Tromp, J., 2009. Adjoint tomography of the southern California crust, *Science,* **325**(5943), 988–992.

Yano, T., Tanimoto, T. & Rivera, L., 2009. The ZH ratio method for long-period seismic data: inversion for S-wave velocity structure, *Geophys. J. Int.,* **179**(1), 413–424.

Yao, H., van Der Hilst, R.D. & Maarten, V., 2006. Surface-wave array tomography in SE Tibet from ambient seismic noise and two-station analysis-I. Phase velocity maps, *Geophys. J. Int.,* **166**(2), 732–744.

Zhu, L. & Rivera, L.A., 2002. A note on the dynamic and static displacements from a point source in multilayered media, *Geophys. J. Int.,* **148**(3), 619–627.

SUPPORTING INFORMATION

Additional Supporting Information may be found in the online version of this paper:

Figure S1. Love waves shown in the tangential-component cross-correlations between N116 and all the yellow stations in Fig. 1.

The cross-correlations filtered to 1 and 5-s period are shown as examples.

Figure S2. Rayleigh waves shown in the vertical and radial component cross-correlations (*Z–Z*, *Z–R*, *R–Z*, and *R–R*) between N116 and all the yellow stations in Fig. 1. (a) Filtered to 1-s period. Both fundamental and higher modes are strong. (b) Filtered to 3-s period. The higher mode is generally stronger in the four profiles. (c) Filtered to 5-s period. Only the fundamental mode is observed.

Figure S3. The Rayleigh wave dispersion and ellipticity (*H*/*V*) calculated for a basin model with a basement at: (a) 6-km depth; (b) 8-km depth. The other model parameters are same as that in Table 1.

Figure S4. The FK synthetics on the waveform in a 1-D basin model in Table 1. The source is at 0.5 km depth with a central period of 3 s. The waveforms are filtered to 3-s period. The top two panels show the *Z* and *R* recordings with a *Z*-directed source. The bottom two panels show the results for R-directed source.
(http://gji.oxfordjournals.org/lookup/suppl/doi:10.1093/gji/ggw235/-/DC1).

Please note: Oxford University Press is not responsible for the content or functionality of any supporting materials supplied by the authors. Any queries (other than missing material) should be directed to the corresponding author for the paper.

APPENDIX A: *H*/*V* RATIO PRESERVE IN CROSS-CORRELATION

To enhance the extraction of surface wave signals, the data of each station are usually pre-processed before cross-correlation (Bensen *et al.* 2007; Lin *et al.* 2014). Here, we show that the Rayleigh wave that emerges in the cross-correlation preserves its *H*/*V* ratio, even with the pre-processing procedures (time domain normalization and spectral whitening) that modify the data.

In time domain normalization, we divide all three components (*Z*/*N*/*E*) by the same trace, which is the smoothed envelope of the data filtered to the earthquake band (use the maximum of the three at each time point). Therefore, the arrival at a certain time t_i is scaled by the same factor (m_i) at all three components. *R* component is the linear combination of *N* and *E*, and therefore is also scaled by the same factor.

The Rayleigh wave in the cross-correlation is from the contribution of all the Rayleigh-wave arrivals from the noise sources at the stationary phase point. For illustration purpose, let us assume those *N* arrivals are spikes. For the *i*th arrival, let the amplitudes recorded at the *Z*/*R* component of the two stations be Z_{i1}/R_{i1} and Z_{i2}/R_{i2}, and be scaled by m_{i1} and m_{i2} during the pre-processing. Then, the *H*/*V* ratio measured from *Z–R* and *Z–Z* cross-correlation is

$$\frac{H}{V} = \frac{\sum_{i=1}^{N} \frac{1}{m_{i1}m_{i2}} Z_{i1} \cdot R_{i2}}{\sum_{i=1}^{N} \frac{1}{m_{i1}m_{i2}} Z_{i1} \cdot Z_{i2}}. \tag{A1}$$

Rayleigh-wave *H*/*V* (*R*/*Z*) ratio is a site property, which is controlled solely by the 1-D structure beneath the seismometer (Tanimoto & Rivera 2008; Yano *et al.* 2009). Let the *H*/*V* ratio at the second station be k_2, then,

$$\frac{R_{i2}}{Z_{i2}} = k_2 \tag{A2}$$

$$\frac{H}{V} = \frac{k_2 \sum_{i=1}^{N} \frac{1}{m_{i1}m_{i2}} Z_{i1} \cdot Z_{i2}}{\sum_{i=1}^{N} \frac{1}{m_{i1}m_{i2}} Z_{i1} \cdot Z_{i2}} = k_2. \tag{A3}$$

We see that the *H*/*V* ratio is preserved in the cross-correlation.

For the spectral whitening in frequency domain, we also do the same operation to all the three components, and the *H*/*V* ratio is also preserved.

APPENDIX B: RAYLEIGH WAVE PARTICLE MOTION WITH BODY WAVE INTERFERENCE

The particle-motion ellipse of the Rayleigh wave is expected to be upright. However, it is observed to be tilted (Figs 4a and b). Here we show that the tilted ellipse can be explained by body wave interference. Let us consider a surface wave signal ($x_s(t)$, $y_s(t)$) interfered by a body wave signal ($x_b(t)$, $y_b(t)$) with phase lag $\Delta\phi$:

$$\begin{cases} x_s(t) = A\cos(wt+\phi) \\ y_s(t) = A\cos(wt+\phi \pm \pi/2)\cdot B \end{cases} \qquad \begin{cases} x_b(t) = C\cos(wt+\phi+\Delta\phi) \\ y_b(t) = C\cos(wt+\phi+\Delta\phi)\cdot D \end{cases}$$

The result is

$$\begin{aligned} x(t) &= x_s(t) + x_b(t) \\ &= A\cos(wt+\phi) + C\left[\cos\Delta\phi\cos(wt+\phi) - \sin\Delta\phi\sin(wt+\phi)\right] \\ &= (A + C\cos\Delta\phi)\cdot\cos(wt+\phi) - (C\sin\Delta\phi)\cdot\sin(wt+\phi) \\ y(t) &= y_s(t) + y_b(t) \\ &= AB\left[\mp\sin(wt+\phi)\right] + CD\left[\cos(wt+\phi)\cdot\cos\Delta\phi - \sin(wt+\phi)\cdot\sin\Delta\phi\right] \\ &= (CD\cos\Delta\phi)\cdot\cos(wt+\phi) - (CD\sin\Delta\phi \pm AB)\cdot\sin(wt+\phi). \end{aligned} \tag{B1}$$

Let

$$a = A + C\cos\Delta\phi$$
$$b = -C\sin\Delta\phi$$
$$c = CD\cos\Delta\phi$$
$$d = -(CD\sin\Delta\phi \pm AB) \tag{B2}$$

and

$$M = \begin{bmatrix} a & b \\ c & d \end{bmatrix},$$

we have

$$\begin{bmatrix} x(t) \\ y(t) \end{bmatrix} = \begin{bmatrix} a & b \\ c & d \end{bmatrix} \begin{bmatrix} \cos(wt+\phi) \\ \sin(wt+\phi) \end{bmatrix} = M \begin{bmatrix} \cos(wt+\phi) \\ \sin(wt+\phi) \end{bmatrix}. \tag{B3}$$

In discrete time $(T_1, \ldots, T_N)$, eq. (B3) is

$$\begin{bmatrix} X_1 & X_2 & \ldots & X_N \\ Y_1 & Y_2 & \ldots & Y_N \end{bmatrix}_{2\times N} = M \begin{bmatrix} \cos(wT_1+\phi) & \cos(wT_2+\phi) & \ldots & \cos(wT_N+\phi) \\ \sin(wT_1+\phi) & \sin(wT_2+\phi) & \ldots & \sin(wT_N+\phi) \end{bmatrix}_{2\times N}.$$

In short,

$$\begin{bmatrix} X_{1\times N} \\ Y_{1\times N} \end{bmatrix} = M \begin{bmatrix} \cos(wT_{1\times N}+\phi) \\ \sin(wT_{1\times N}+\phi) \end{bmatrix}_{2\times N}. \tag{B4}$$

With the singular value decomposition of M, eq. (B4) is

$$\begin{bmatrix} X_{1\times N} \\ Y_{1\times N} \end{bmatrix} = U_{2\times 2}\Sigma_{2\times 2}V^T_{2\times 2} \begin{bmatrix} \cos(wT_{1\times N}+\phi) \\ \sin(wT_{1\times N}+\phi) \end{bmatrix}_{2\times N}, \tag{B5}$$

where U and V are orthonormal matrices, and Σ is a diagonal matrix.

We recognize that the particle motion described by $\left[\begin{smallmatrix} \cos(wT_{1\times N}+\phi) \\ \sin(wT_{1\times N}+\phi) \end{smallmatrix}\right]$ is a circle, V^T performs a rotation on the circle and the result remains a circle. The circle is then stretched to an ellipse with the operation of Σ, and finally, the ellipse is rotated by the operator U.

Therefore, we should expect to observe a tilted particle-motion ellipse of the surface wave, if it is interfered by the body wave.

Here we show an example.

Let $A = 1$, $B = 2$, $\phi = 0$, $C = 0.2$, A $= 0.5$, $D = \tan(\pi/3)$, $\Delta\phi = \pi/9$.

The period $T = 6$ s and $w = 2\pi/T$. We plot one period, with sampling period $dt = 0.01$ s. The result is shown below.

We proceed to show that the matrix M can be determined from the observation $\left[\begin{smallmatrix} X \\ Y \end{smallmatrix}\right]$.

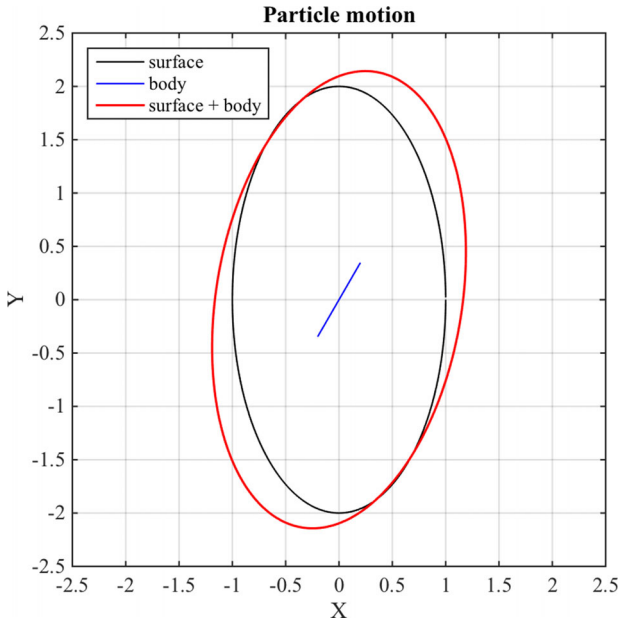

Let $R = \begin{bmatrix} \cos(wT_{1\times N} + \phi) \\ \sin(wT_{1\times N} + \phi) \end{bmatrix}$

since

$$\int_0^{nT} \cos^2 wt\,\mathrm{d}t = \int_0^{nT} \sin^2 wt\,\mathrm{d}t = nT/2 \quad \int_0^{nT} \cos wt \sin wt\,\mathrm{d}t = 0, \tag{B6}$$

where $T = 2\pi/w$ is the period, n is the number of periods.

Then, if the observation evenly samples integer number of periods (with N samples), we have

$$RR^T = \begin{bmatrix} N/2 & \\ & N/2 \end{bmatrix}. \tag{B7}$$

Recall that

$$\begin{bmatrix} X \\ Y \end{bmatrix} = MR.$$

Then

$$\begin{bmatrix} X \\ Y \end{bmatrix} R^T = MRR^T = M \begin{bmatrix} N/2 & \\ & N/2 \end{bmatrix}$$

$$\begin{aligned} M &= 2/N \begin{bmatrix} X \\ Y \end{bmatrix}_{2\times N} R^T \\ &= 2/N \begin{bmatrix} X \\ Y \end{bmatrix}_{2\times N} \begin{bmatrix} \cos(wT_{N\times 1} + \phi) & \sin(wT_{N\times 1} + \phi) \end{bmatrix}_{N\times 2}. \end{aligned} \tag{B8}$$

The exact ϕ is unknown, because our phase measurement $\tilde{\phi}$ is based on 'contaminated' data. However, we can assume a weak body wave interference, and $\phi \approx \tilde{\phi}$.

Known M thus a, b, c, d, we are unable to recover the surface wave and body wave signals uniquely since there exist five parameters (A, B, C, D, $\Delta\phi$), unless we have constraint on at least one of them.